SUPPORTING INFORMATION

Cobalt Catalysts for the Conversion of CO_2 to light Hydrocarbons at Atmospheric Pressure

Rhodri E. Owen, Justin P. O'Byrne, Davide Mattia, Sofia I. Pascu, Pawel Plucinski and Matthew D. Jones.

Table of contents:

Reactor Setup

Figure 1. Schematic showing the construction of the reactor used for catalyst tests.

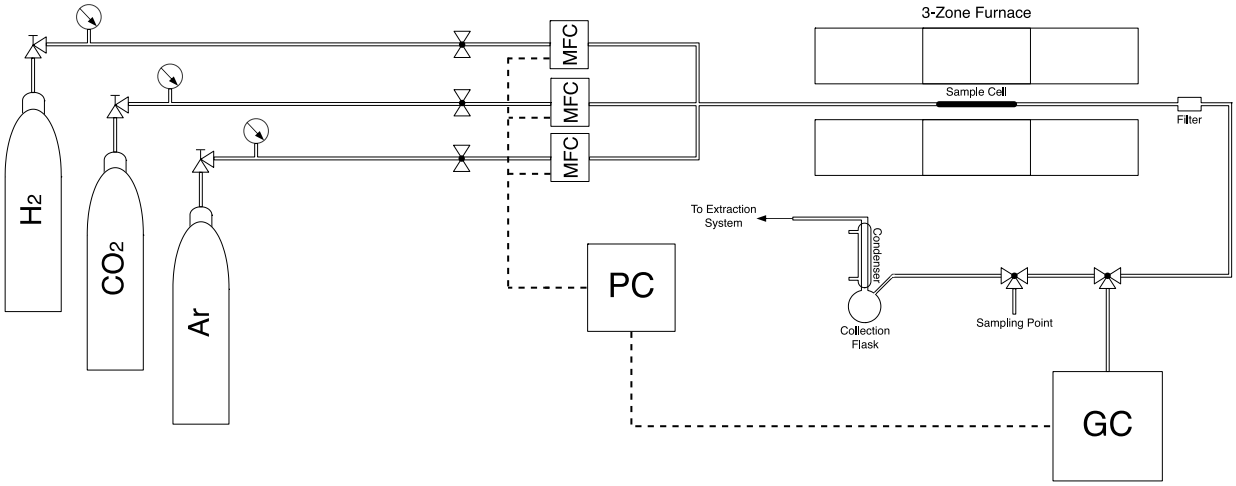

Note: the online GC is only equipped with an FID and as a result was used only to monitor hydrocarbon selectivity/production during the reaction and not used for any calculations. All selectivities and conversions were calculated using an offline GC-MS system: Agilent 7890A equipped with a thermal conductivity detector (TCD), a flame ionisation detector (FID) and a 5975C EI mass spectrometer (MS).

Catalyst Testing Procedure

The same general catalyst testing procedure was repeated for all catalyst tests and is detailed below.

- 0.7 g of the chosen catalyst is packed into the reactor sample cell, 130 mm in length, internal diameter 1.58 mm. Quartz wool is used to hold the sample in place under flow conditions.
- The sample cell is placed in the centre of a tubular furnace and connected to the rest of the reactor.
- The furnace is heated to the pre-treatment temperature of 300^{o}C under a flow of argon at a ramp rate of 10^{o}C min^{-1}.
- Once at temperature the argon flow is replaced with a flow of hydrogen and left to reduce for 2 hours (unless otherwise stated).
- With the pre-treatment time completed hydrogen flow is reduced and a flow of carbon dioxide introduced in a 3:1, H_2:CO_2 ratio.

- After one hour on stream a gas sample is collected from the sampling point with a gas tight syringe.
- Each sample is then analysed with an off line GC-MS system (details given above) with a HP-PLOT/Q column, 30 m in length with an internal diameter of 0.530 mm.
- Sample collection is repeated every hour until the catalyst test is completed.
- Once testing is complete hydrogen and carbon dioxide flow is stopped and replaced with a flow of argon which remains on until the furnace has cooled to a safe temperature.

Typical Catalyst Preparation Procedure

The catalysts investigated were all prepared using the same general procedure detailed below. The masses of the metal salts added are detailed in Table 1.

2 g of the desired silica support (SiO_2 with a pore size of 60, 250 or 500 Å and a particle size of 35-70 μm or 1-2 mm) was suspended in the minimum amount of methanol. To this suspension the appropriate mass of $Co(NO_3)_3 \cdot 6H_2O$ in 20 cm^3 methanol was added drop-wise while being stirred. Following this step the required amount of each promoter's precursor ($Pd(OAc)_2$, K(OAc), Li(OAc), $Na(OAc) \cdot 3H_2O$, $PtCl_2$, $RuCl_3 \cdot xH_2O$, $CrCl_3$ and $Mn(OAc)_3 \cdot 2H_2O$) dissolved in methanol (note: for $(NH_4)_6Mo_7O_{24} \cdot 4H_2O$, which is not soluble in methanol, the minimum amount of deionised water was used) was also added slowly to afford the desired cobalt:promoter ratio. The resulting mixture was stirred for 10 minutes before being sonicated for 60 minutes.

The solvent was removed under vacuum while being heated through the use of a rotary evaporator until a powder of constant mass was obtained. The resulting powder was then calcined in air for 16 hour at 723 K

Table 1. The salts and masses of each used in the preparation of each catalyst system (each value given is for 2g of silica support).

Catalyst[a]	Mass of $Co(NO_3)_2 \cdot 6H_2O$ Used / g	2nd Metal Salt Used	Mass of 2nd Metal Salt Used / g	3rd Metal Salt Used	Mass of 3rd Metal Salt Used / g
20wt%Co	2.47	N/A	N/A	N/A	N/A
20wt%Co/1wt%Pd	2.50	$Pd(OAc)_2$	0.0534	N/A	N/A
10wt%Co/1wt%Pd/1wt%K	1.12	$Pd(OAc)_2$	0.0479	K(OAc)	0.0570
20wt%Co/1wt%Pd/1wt%K	2.53	$Pd(OAc)_2$	0.0541	K(OAc)	0.0644
40wt%Co/1wt%Pd/1wt%K	6.81	$Pd(OAc)_2$	0.0727	K(OAc)	0.0866
20wt%Co/1wt%Pd/0.5wt%K	2.52	$Pd(OAc)_2$	0.0538	K(OAc)	0.0320
20wt%Co/1wt%Pd/1.5wt%K	2.55	$Pd(OAc)_2$	0.0544	K(OAc)	0.0972
20wt%Co/1wt%Pd/3wt%K	2.60	$Pd(OAc)_2$	0.0555	K(OAc)	0.1982
20wt%Co/1wt%K	2.50	K(OAc)	0.0635	N/A	N/A
20wt%Co/1wt%Pd/1wt%K_250	2.53	$Pd(OAc)_2$	0.0541	K(OAc)	0.0644
20wt%Co/1wt%Pd/1wt%K_500	2.53	$Pd(OAc)_2$	0.0541	K(OAc)	0.0644
20wt%Co/1wt%Pd/1wt%K_60[b]	2.53	$Pd(OAc)_2$	0.0541	K(OAc)	0.0644
20wt%Co/1wt%Pd/1wt%Li_500	2.53	$Pd(OAc)_2$	0.0541	Li(OAc)	0.3777
20wt%Co/1wt%Pd/1wt%Na_500	2.53	$Pd(OAc)_2$	0.0541	$Na(OAc) \cdot 3H_2O$	0.0916
20wt%Co/1wt%Pt/1wt%K_500	2.53	$PtCl_2$	0.0350	K(OAc)	0.0644
20wt%Co/1wt%Ru/1wt%K_500	2.53	$RuCl_3 \cdot xH_2O$	0.0663	K(OAc)	0.0644
20wt%Co_500	2.47	N/A	N/A	N/A	N/A
20wt%Co/1wt%Li_500	2.50	Li(OAc)	0.3729	N/A	N/A
20wt%Co/1wt%Na_500	2.50	$Na(OAc) \cdot 3H_2O$	0.0904	N/A	N/A
20wt%Co/1wt%K_500	2.50	K(OAc)	0.0635	N/A	N/A
20wt%Co/1wt%Mo_500	2.50	$(NH_4)_6Mo_7O_{24} \cdot 4H_2O$	0.0466	N/A	N/A
20wt%Co/1wt%Cr_500	2.50	$CrCl_3$	0.0598	N/A	N/A
20wt%Co/1wt%Mn_500	2.50	$Mn(OAc)_3 \cdot 2H_2O$	0.0622	N/A	N/A
20wt%Co/1wt%Na/1wt%Mn_500	2.53	$Mn(OAc)_3 \cdot 2H_2O$	0.0630	$Na(OAc) \cdot 3H_2O$	0.0916
20wt%Co/1wt%Na/1wt%Mo_500	2.53	$(NH_4)_6Mo_7O_{24} \cdot 4H_2O$	0.0472	$Na(OAc) \cdot 3H_2O$	0.0916

[a]Metal nanoparticles supported on SiO_2_X where X represents the pore diameter of the SiO_2. [b] SiO_2 particle size 1-2 mm (N.B. all other SiO_2 are in the range 35-70 μm).

Equations Used to Calculate Conversion, Selectivity and Carbon Balance:

Carbon balance was calculated using the following:

$$Balance = \frac{Total\ Moles\ of\ Carbon\ in\ Product\ Stream\ /\ hr}{Total\ Moles\ of\ Carbon\ Added\ /\ hr}\ X\ 100$$

The conversion was determined using the following:

$$Conversion = \frac{Moles\ of\ CO_{2\ in} - Moles\ of\ CO_{2\ out}}{Moles\ of\ CO_{2\ in}}\ X\ 100$$

Selectivities were determined using the following:

$$Selectivity\ of\ Product\ x = \frac{Moles\ of\ Carbon\ in\ Product\ x}{Moles\ of\ CO_2\ Converted}\ X\ 100$$

SEM/EDX Analysis Results

SEM was carried out on a JEOL 6480LV at 5 - 25 kV. Energy-dispersive X-ray spectroscopy (EDS) was carried out *in-situ* during SEM analysis. Images and spectra obtained for 20wt%Co/1wt%Pd/1wt%K/SiO_2_60 are shown in Figure 2.

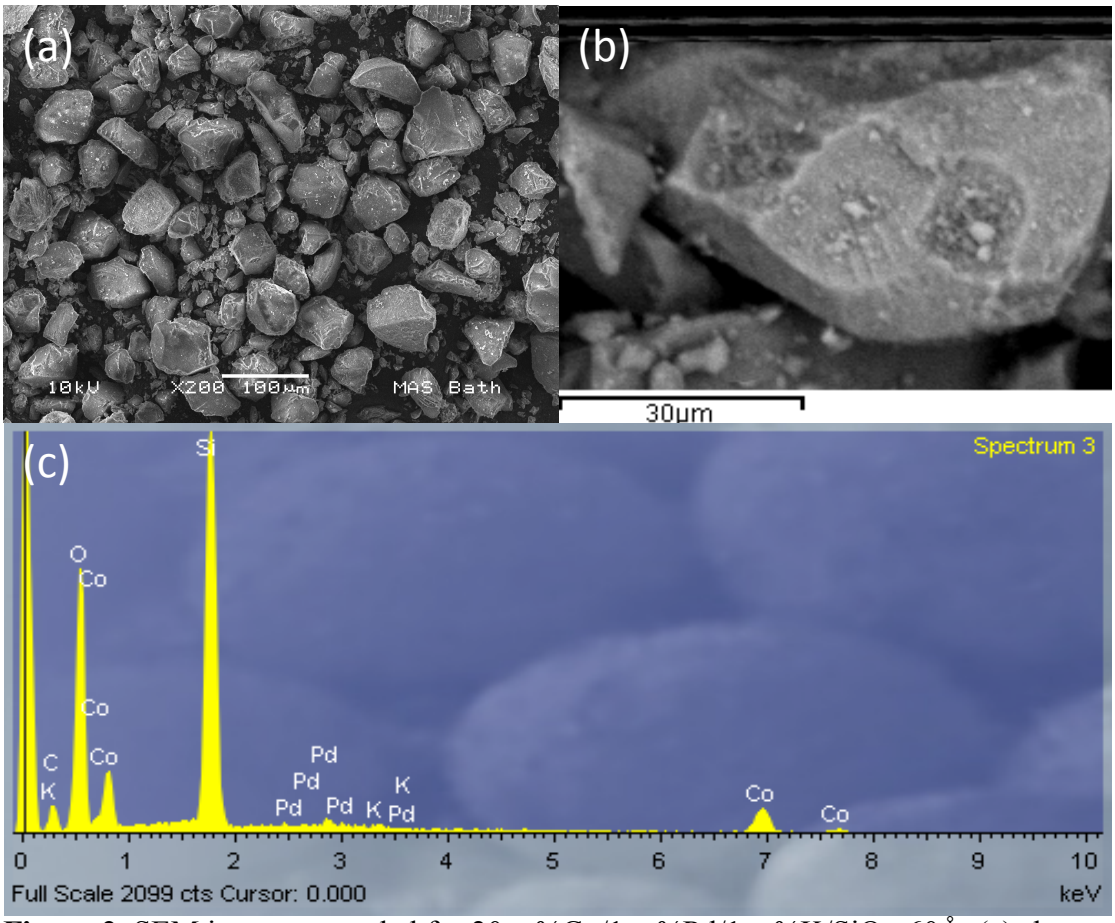

Figure 2. SEM images recorded for 20wt%Co/1wt%Pd/1wt%K/SiO_2-60Å. (a) shows the overall catalyst morphology with (b) showing the same catalyst at a higher magnification. (c) EDX spectra recorded in conjunction with SEM (b).

TEM Analysis Results

Transmission electron microscopy (TEM) carried out using a JEOL 1200 operated at 120 kV. Samples for TEM analysis were prepared in ethanol and deposited onto copper or nickel grids. TEM images recorded for 20wt%Co/SiO_2_60 are shown in Figure 3. The images recorded for 20wt%Co/1wt%Pd/1wt%K/SiO_2_60 are shown in Figure 4. TEMs showing the influence of pore size on the silica for the 20wt%Co/1wt%Pd/1wt%K/SiO_2 catalyst system is shown in Figure 5. The effects on catalyst morphology when varying alkali metal in the 20wt%Co/1wt%Pd/1wt%M/SiO_2_500 catalyst system, where M = Li, Na and K, are shown in Figure 6. The effects on catalyst morphology when varying the noble metal in the 20wt%Co/1wt%M/1wt%K/SiO_2_500 catalyst system, where M = Pd, Ru and Pt, are shown in Figure 7.

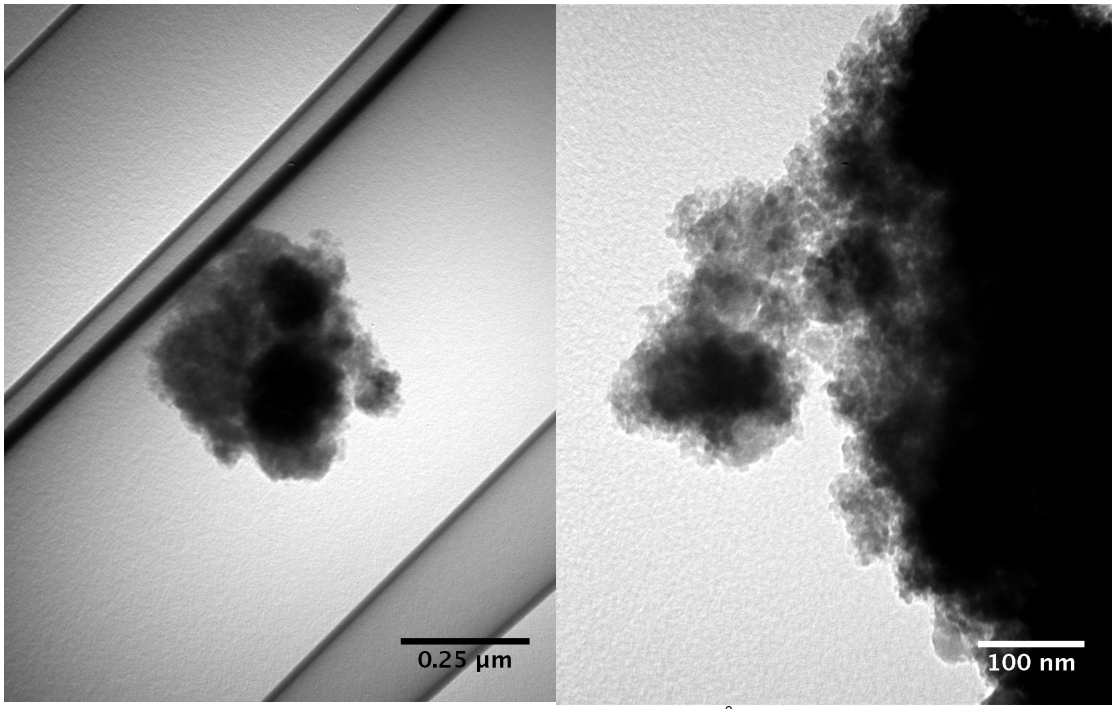

Figure 3. TEM images recorded for 20wt%Co/SiO_2-60Å at two different magnifications.

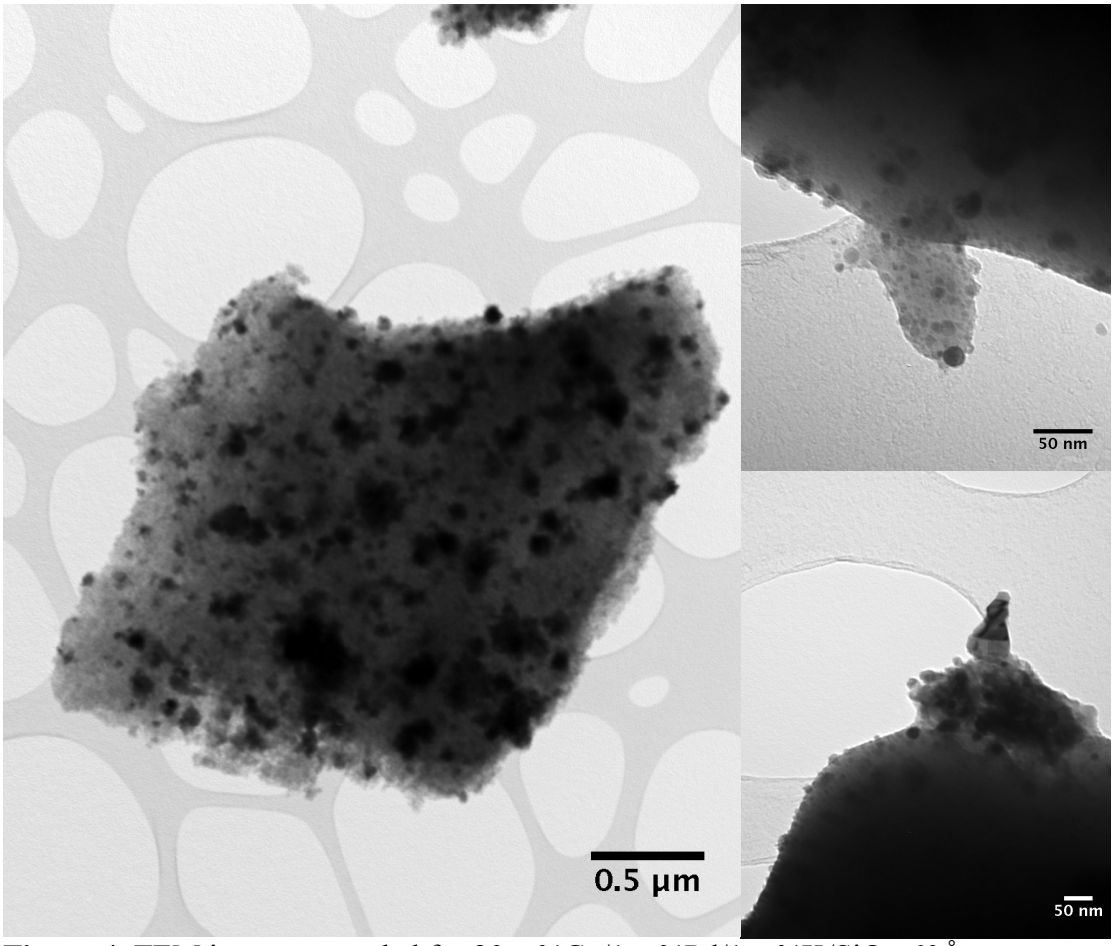

Figure 4. TEM images recorded for 20wt%Co/1wt%Pd/1wt%K/SiO_2-60Å.

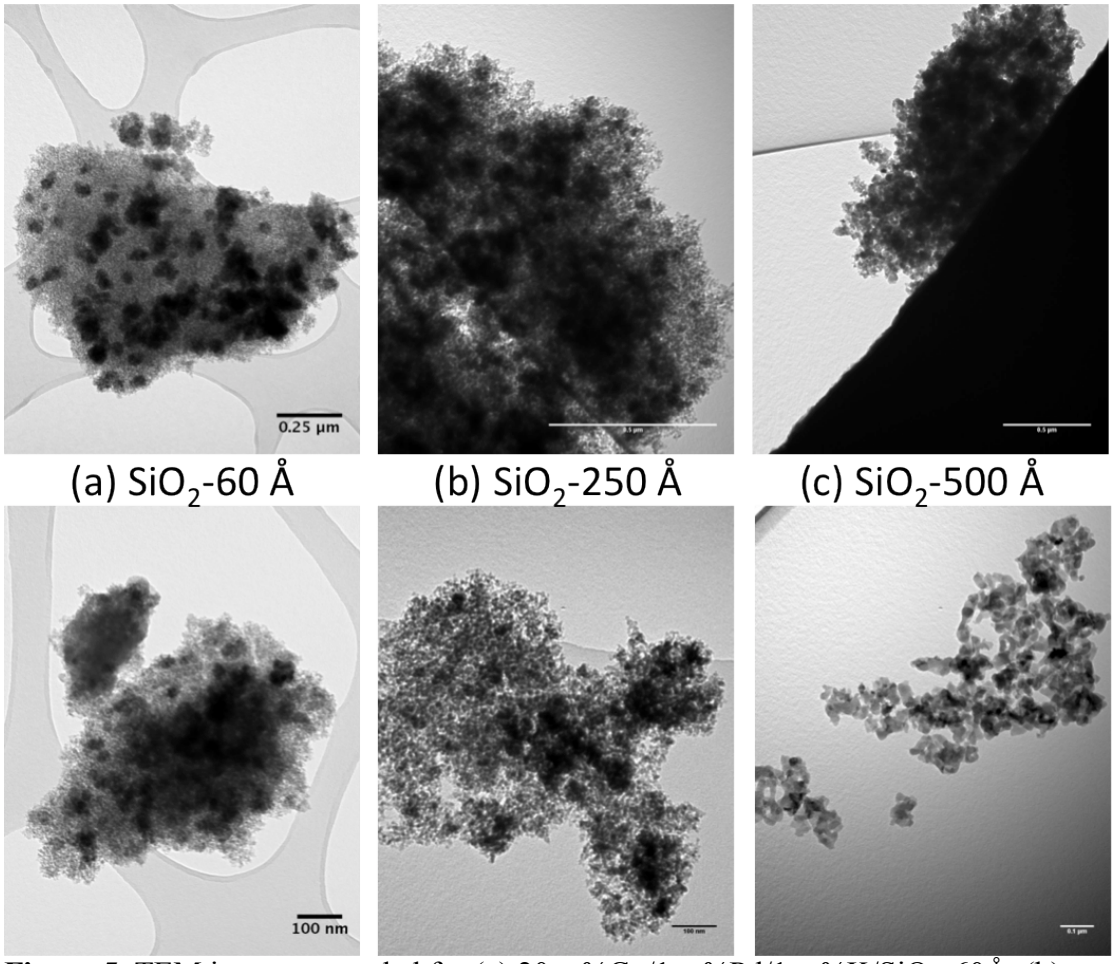

Figure 5. TEM images recorded for (a) 20wt%Co/1wt%Pd/1wt%K/SiO_2-60Å, (b) 20wt%Co/1wt%Pd/1wt%K/SiO_2-250Å and (c) 20wt%Co/1wt%Pd/1wt%K/SiO_2-500Å.

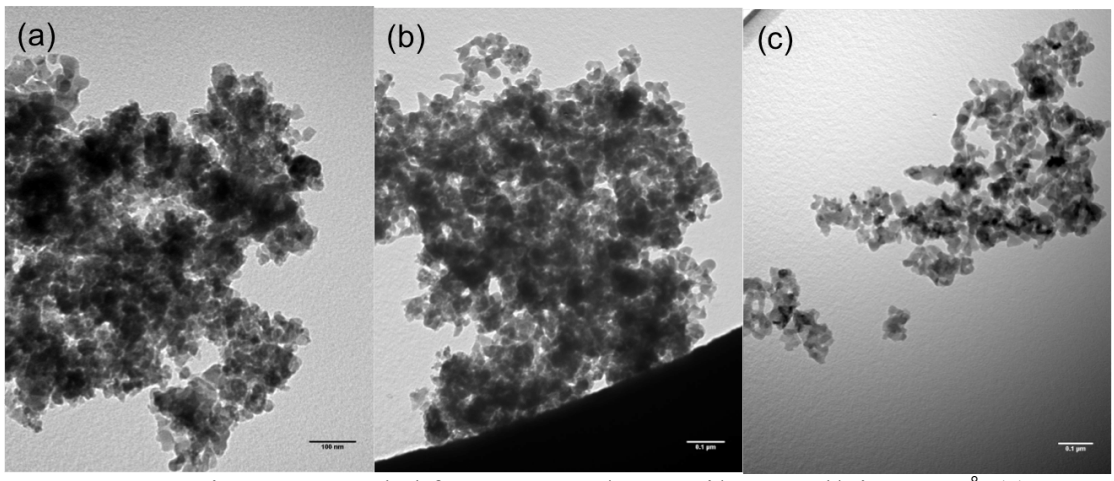

Figure 6. TEM images recorded for 20wt%Co/1wt%Li/1wt%Pd/SiO_2-500Å (a) 20wt%Co/1wt%Na/1wt%Pd/SiO_2-500Å (b) and 20wt%Co/1wt%K/1wt%Pd/SiO_2-500Å.

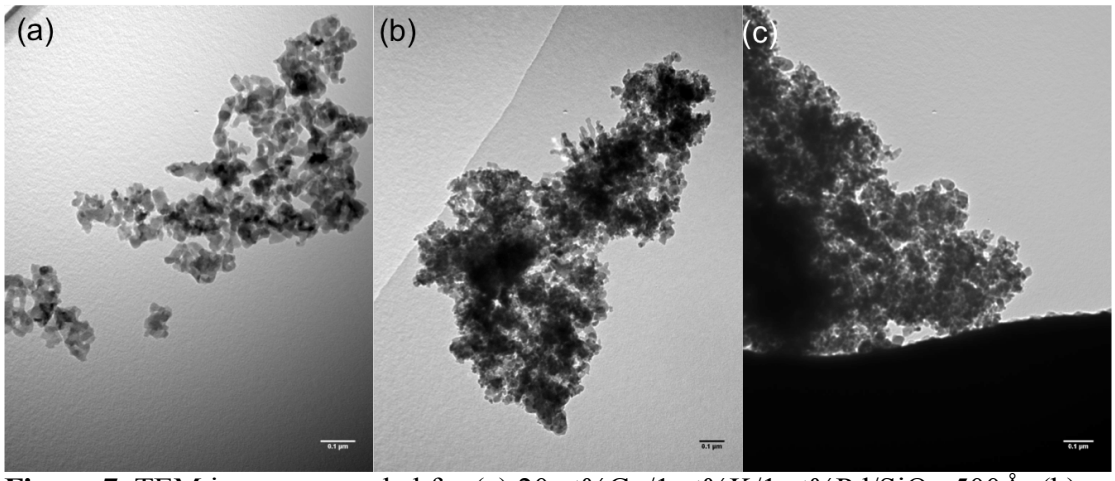

Figure 7. TEM images recorded for (a) 20wt%Co/1wt%K/1wt%Pd/SiO_2-500Å, (b) 20wt%Co/1wt%K/1wt%Pt/SiO_2-500Å and (c) 20wt%Co/1wt%K/1wt%Ru/SiO_2-500Å

N_2 Physisorption Analysis Results

N_2 physisorption analysis was carried out using a BELSORP-Mini II (BEL Japan). Prior to measurements the catalyst samples were degassed at 300°C for 4 hours. Catalyst surface areas were determined by the Brunauer-Emmett-Teller (BET) method. The results are summarised in Table 2.

Table 2. The BET surface areas and average pore size recorded for the catalyst systems

Catalyst[a]	BET Surface Area / m^2g^{-1}
20wt%Co/SiO_2_60	340
20wt%Co/1wt%Pd/SiO_2_60	289
20wt%Co/1wt%K/SiO_2_60	294
20wt%Co/1wt%K/1wt%Pd/SiO_2_60	248
20wt%Co/1wt%K/1wt%Pd/SiO_2_60[b]	286
20wt%Co/1wt%K/1wt%Pd/SiO_2_250	186
20wt%Co/1wt%K/1wt%Pd/SiO_2_500	66.1
20wt%Co/1wt%Li/1wt%Pd/SiO_2_500	60.8
20wt%Co/1wt%Na/1wt%Pd/SiO_2_500	56.2
20wt%Co/1wt%K/1wt%Pt/SiO_2_500	83.5
20wt%Co/1wt%K/1wt%Ru/SiO_2_500	71.9
20wt%Co/SiO_2_500	62.8
20wt%Co/1wt%Li/SiO_2_500	58.3
20wt%Co/1wt%Na/SiO_2_500	58.1
20wt%Co/1wt%K/SiO_2_500	62.8
20wt%Co/1wt%Mo/SiO_2_500	74.8
20wt%Co/1wt%Cr/SiO_2_500	68.4
20wt%Co/1wt%Mn/SiO_2_500	62.3
20wt%Co/1wt%Na/1wt%Mn/SiO_2_500	61.2
20wt%Co/1wt%Na/1wt%Mo/SiO_2_500	56.6

[a]Metal nanoparticles supported on SiO_2_X where X represents the pore diameter of the SiO_2. [b] SiO_2 particle size 1-2 mm (N.B. all other SiO_2 are in the range 35-70 μm)

pXRD Analysis Results

pXRD were recorded on a BRUKER D8-Advance diffractometer from 2θ = 4º to 60 º, with a step size of 0.0164 º, using CuKα (λ = 1.5406 Å) radiation. These samples were collected using the diffractometer set up in capillary mode, step time 0.3s.

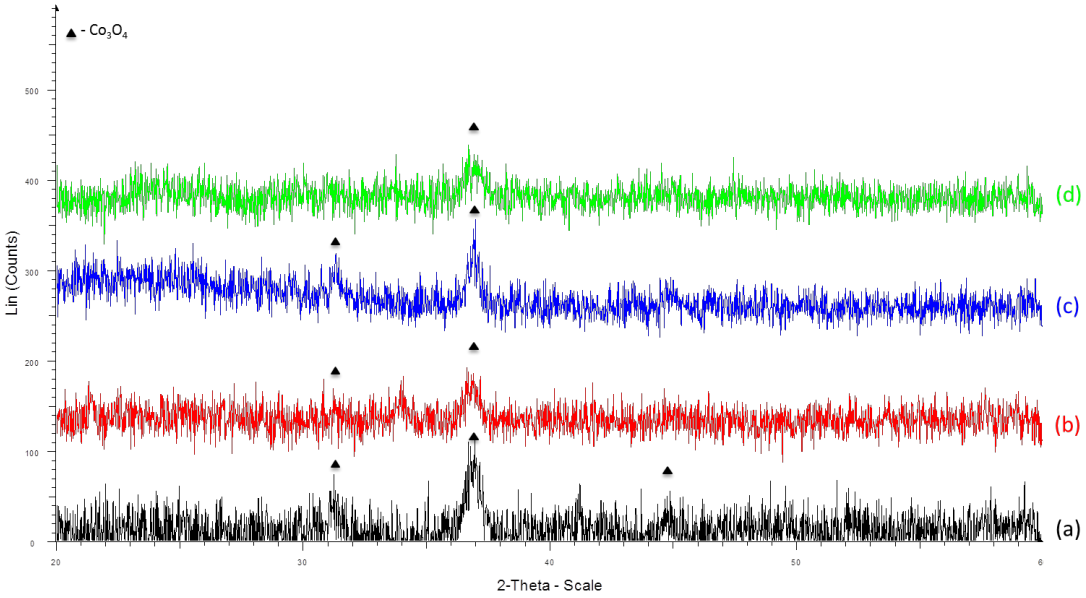

Figure 8. pXRD patterns recorded for (a) 20wt%Co/SiO_2-60Å, (b) 20wt%Co/1wt%Pd/SiO_2-60Å, (c) 20wt%Co/1wt%K/SiO_2-60Å and (d) 20wt%Co/1wt%Pd/1wt%K/SiO_2-60Å.

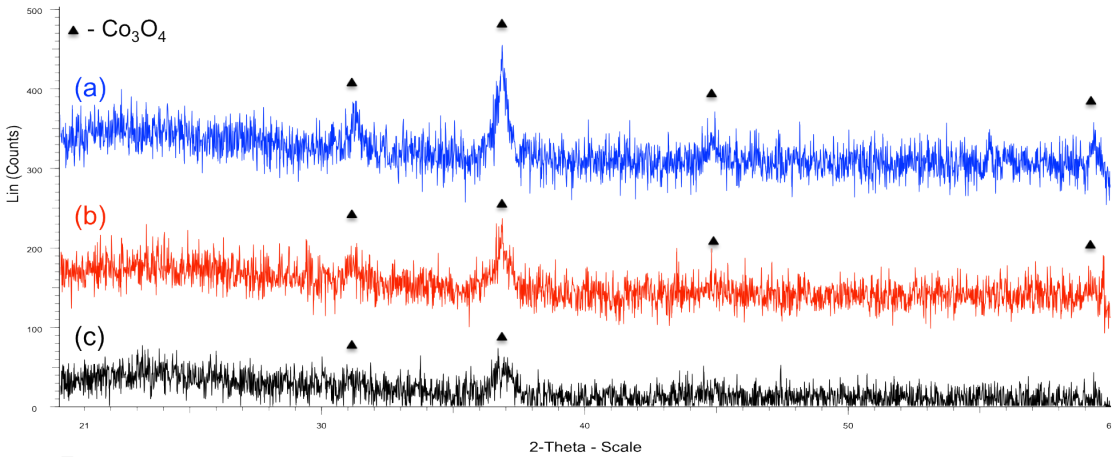

Figure 9. pXRD patterns recorded for (a) 20wt%Co/1wt%Pd/1wt%K/SiO_2-500Å, (b) 20wt%Co/1wt%Pd/1wt%K/SiO_2-250Å and (c) 20wt%Co/1wt%Pd/1wt%K/SiO_2-60Å.

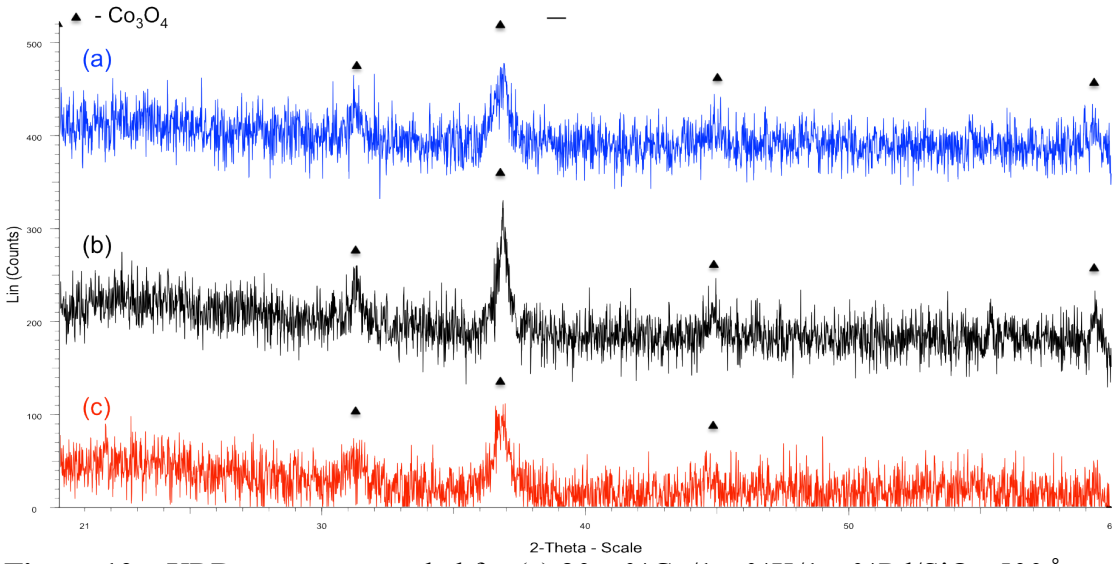

Figure 10. pXRD patterns recorded for (a) 20wt%Co/1wt%K/1wt%Pd/SiO_2-500Å, (b) 20wt%Co/1wt%K/1wt%Pt/SiO_2-500Å and (c) 20wt%Co/1wt%K/1wt%Ru/SiO_2-500Å.

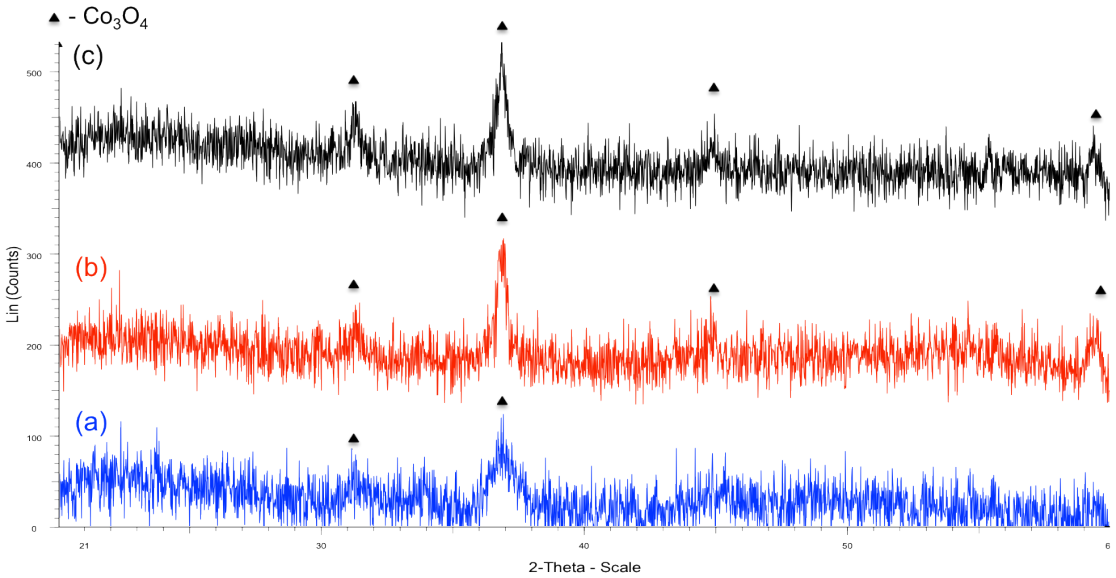

Figure 11. pXRD patterns recorded for (a) 20wt%Co/1wt%Li/1wt%Pd/SiO_2-500Å, (b) 20wt%Co/1wt%Na/1wt%Pd/SiO_2-500Å and (c) 20wt%Co/1wt%K/1wt%Pd/SiO_2-500Å.

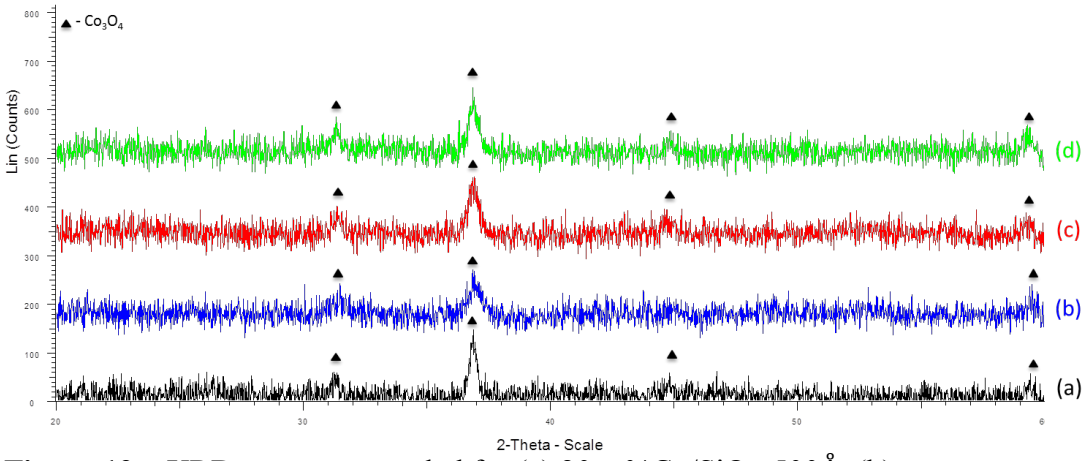

Figure 12. pXRD patterns recorded for (a) 20wt%Co/SiO_2-500Å, (b) 20wt%Co/1wt%Li/SiO_2-500Å, (c) 20wt%Co/1wt%Na/SiO_2-500Å and (d) 20wt%Co/1wt%K/SiO_2-500Å.

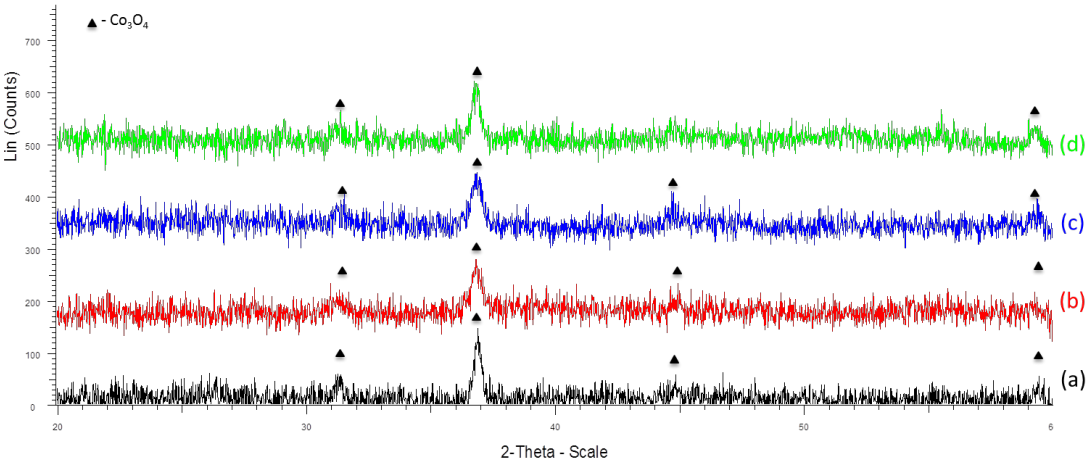

Figure 13. pXRD patterns recorded for (a) 20wt%Co/SiO_2-500Å, (b) 20wt%Co/1wt%Mn/SiO_2-500Å, (c) 20wt%Co/1wt%Mo/SiO_2-500Å and (d) 20wt%Co/1wt%Cr/SiO_2-500Å

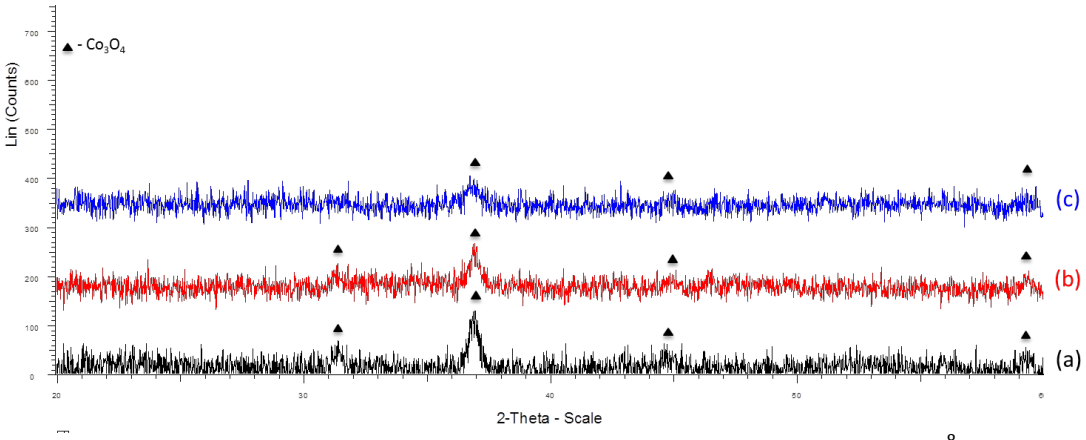

Figure 14. pXRD patterns recorded for (a) 20wt%Co/1wt%Na/SiO_2-500Å, (b) 20wt%Co/1wt%Na/1wt%Mo/SiO_2-500Å and (c) 20wt%Co/1wt%Na/1wt%Mn/SiO_2-500Å.

Particle Size Analysis

In order to gain further insight into the effect of support and promoters on each catalyst system the effect on particle size was investigated. For selected catalyst systems XRD was used to calculate crystallite size.

Particle Size Calculated from pXRD.

For the calculation of crystallite size from pXRD selected catalysts were run on a BRUKER D8-Advance diffractometer in flat plate mode over a 2θ range of 4º to 60 º, with a step size of 0.0164 º, 0.6 s per step, using CuKα (λ = 1.5406 Å) radiation. Crystallite size was calculated using the Sherrer equation from the (311) Co_3O_4 peak. The calculated values are shown in Table 3.

Table 3. Particle sizes calculated from pXRD.

Entry	Catalyst[a]	XRD - D_p [a] (nm)	C_{5+} Selectivity
1	20wt%Co/1wt%Pd/1wt%K_60	8.4	0
2	20wt%Co/1wt%Pd/1wt%K_250	9.4	1.1
3	20wt%Co/1wt%Pd/1wt%K_500	14.0	3.7
4	20wt%Co/1wt%Ru/1wt%K_500	12.0	6.5
5	20wt%Co/1wt%Pt/1wt%K_500	10.5	12.1
6	20wt%Co/1wt%Pd/1wt%Li_500	10.1	2.4
7	20wt%Co/1wt%Pd/1wt%Na_500	14.0	9.2
8	20wt%Co_500	16.8	0
9	20wt%Co/1wt%Li_500	9.3	0.6
10	20wt%Co/1wt%K_500	12.0	4.4
11	20wt%Co/1wt%Na_500	12.0	6.4
12	20wt%Co/1wt%Mo_500	9.3	0
13	20wt%Co/1wt%Na/1wt%Mo_500	12.0	10.4

a-calculated from pXRD using the Scherrer Equation.

The size of the crystalline phases calculated for entries **1-3** (same metal loadings, but different support) appears to increase as the C_{5+} selectivity increases. This is in agreement with previous work which has shown the particle size is intrinsically linked to heavier HC production.[1] A similar trend is observed if entry **6** is compared to **7**. The same trend is further observed for **9** vs **10/11**. This emphasises that crystal size is important but, in this case, is not solely responsible for the selectivities observed and we believe there are subtle effects from the addition of promoters.

XPS analysis

The Kratos AXIS 165 spectrometer was used for measurements with the following parameters:

Sample Temperature: 20-30 ^{o}C

X-Ray Gun: mono Al K_{α} 1486.58 eV; 150 W (10 mA, 15kV),

Pass Energy: 160 eV for survey spectra and 20 eV for narrow regions

Step: 1 eV (survey), 0.05 eV (regions)

Dwell: 50ms (survey), 100 ms (regions)

Sweeps: survey (~4), narrow regions (5-45)

Calibration: the C 1s line at 284.8 eV was used as charge reference.

Other: spectra were collected in the normal to the surface.

XPS detection limit is estimated to be ~0.1 at%.

Data processing: Construction and peak fitting of synthetic peaks in narrow region spectra used a Shirely type background and the synthetic peaks were of a mixed Gaussian-Lorenzian type. Relative sensitivity factors used are from CasaXPS library containing Scofield cross-sections.

The XPS results obtained are summarised in the Table 4 and the following Figures (Fig 15-23)

Catalyst	Binding Energy (eV)			Composition (atom %)					
20wt%Co/1wt%Pd/1wt%K/SiO_2-60Å	**Co 2p**	**Pd 3d**	**K 2p**	**Co**	**Pd**	**K**	**Si**	**C**	**O**
	779.75	336.75	395.75	1.359	0.243	0.267	30.864	3.669	63.598
20wt%Co/1wt%Pd/1wt%K/SiO_2-500Å	**Co2p**		**Pd 3d**	**Co**		**Pd**	**Si**	**C**	**O**
	779.96		335.96	0.44		0.33	41.95	1.23	56.05
20wt%Co/1wt%Pd/1wt%Li/SiO_2-500Å	**Co 2p**	**Pd 3d**		**Co**		**Pd**	**Si**	**C**	**O**
	779.97	336.97		0.919		0.043	21.52	13.611	59.622
20wt%Co/1wt%Pd/1wt%Na/SiO_2-500Å	**Co 2p**	**Pd 3d**	**Na 1s**	**Co**	**Pd**	**Na**	**Si**	**O**	**C**
	779.93	336.93	1070.93	0.890	0.108	1.558	21.878	57.984	13.206
20wt%Co/1wt%Pt/1wt%K/SiO_2-500Å	**Co 2p**	**Pt 4d**	**K 2p**	**Co**	**Pt**	**K**	**Si**	**O**	**C**
	780.07	74.07	293.07	1.678	0.161	0.505	26.986	67.126	3.545
20wt%Co/1wt%Ru/1wt%K/SiO_2-500Å	**Co 2p**		**K 2p**	**Co**		**K**	**Si**	**O**	**C**
	780.01		294.01	1.758		0.600	26.643	66.430	4.569
20wt%Co/1wt%Li/SiO_2-500Å	**Co 2p**			**Co**			**Si**	**O**	**C**
	779.93			1.370			25.799	66.545	6.286
20wt%Co/1wt%Na/SiO_2-500Å	**Co 2p**	**Na 1s**		**Co**		**Na**	**Si**	**O**	**C**
	779.84	1071.84		0.810		1.837	26.186	64.065	7.102
20wt%Co/1wt%K/SiO_2-500Å	**Co 2p**		**K 2p**	**Co**		**K**	**Si**	**O**	**C**
	779.91		292.91	1.031		0.683	27.051	66.598	4.636
20wt%Co/1wt%Na/1wt%Mo/SiO_2-500Å	**Co 2p**	**Na 1s**	**Mo 3d**	**Co**	**Na**	**Mo**	**Si**	**O**	**C**
	779.95	1070.95	231.95	1.424	1.649	0.334	26.046	64.061	6.486

Table 4. A summary of the XPS results recorded for selected catalyst systems

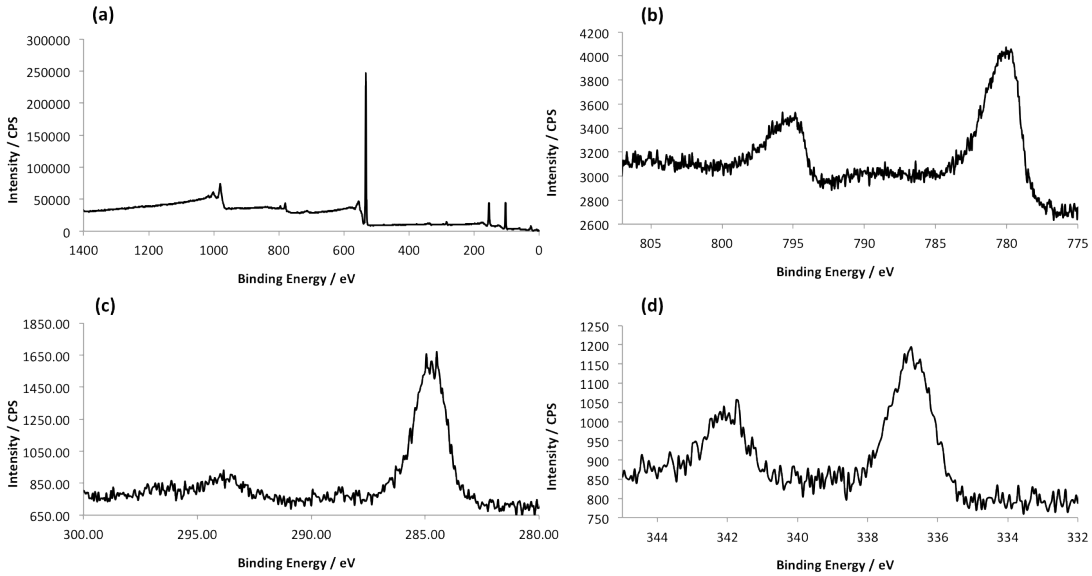

Figure 15. XPS spectra recorded for 20wt%Co/1wt%Pd/1wt%K/SiO_2-60Å. (a) Shows the survey spectrum, (b) Shows the Co 2p region indicating the presence of Co_3O_4, (c) Shows the K 2p region indicating that K is present as K_2O. Note that the peak present at 284.7 eV is the C 1s peak and the smaller peak at 293.3 eV is attributed to K 2p. (d) Shows the Pd 3d region indicating that Pd is present as PdO.

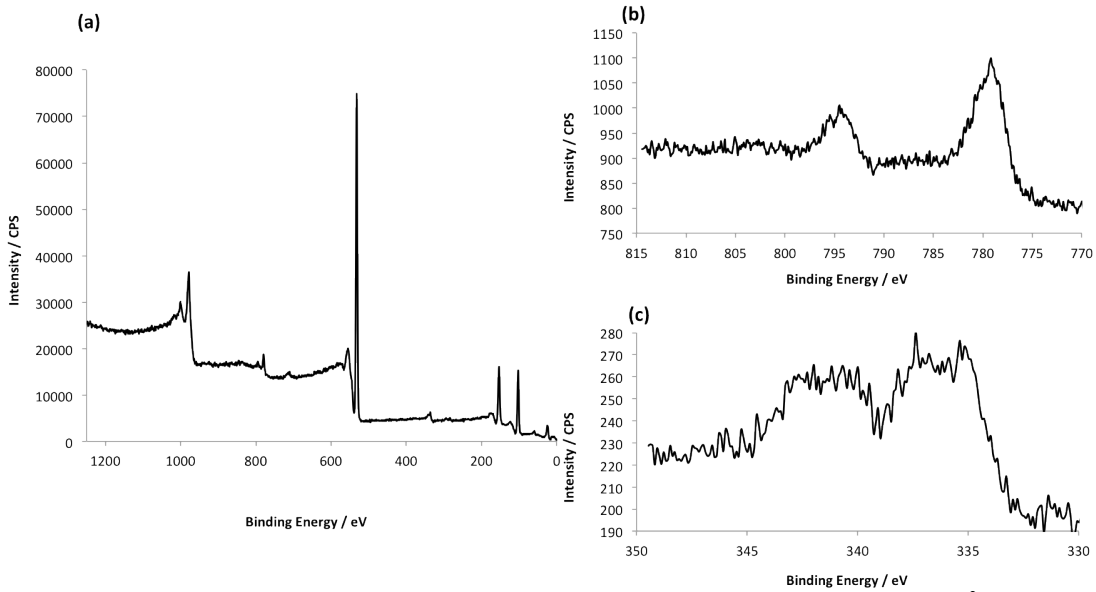

Figure 16. XPS spectra recorded for 20wt%Co/1wt%Pd/1wt%K/SiO_2-500Å. (a) survey spectrum. (b) Co 2p region showing the presence of Co as Co_3O_4. (c) Pd 3d region showing the presence of Pd as PdO. No peaks attributable to potassium could be detected.

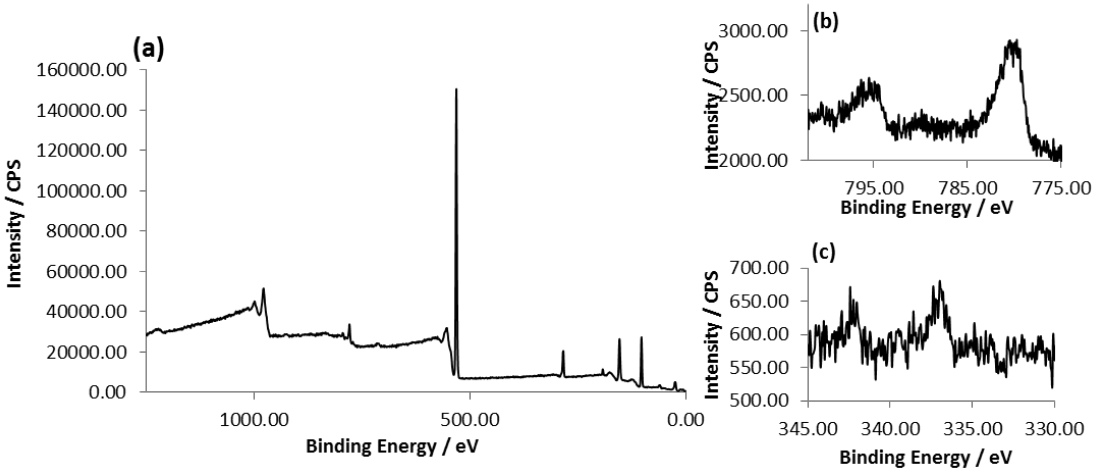

Figure 17. XPS spectra recorded for 20wt%Co/1wt%Pd/1wt%Li/SiO_2-500Å. (a) Survey spectrum. (b) Co 2p region showing the presence of Co as Co_3O_4. (c) Pd 3d region showing the presence of Pd as PdO. No peaks attributable to any lithium species were detectable.

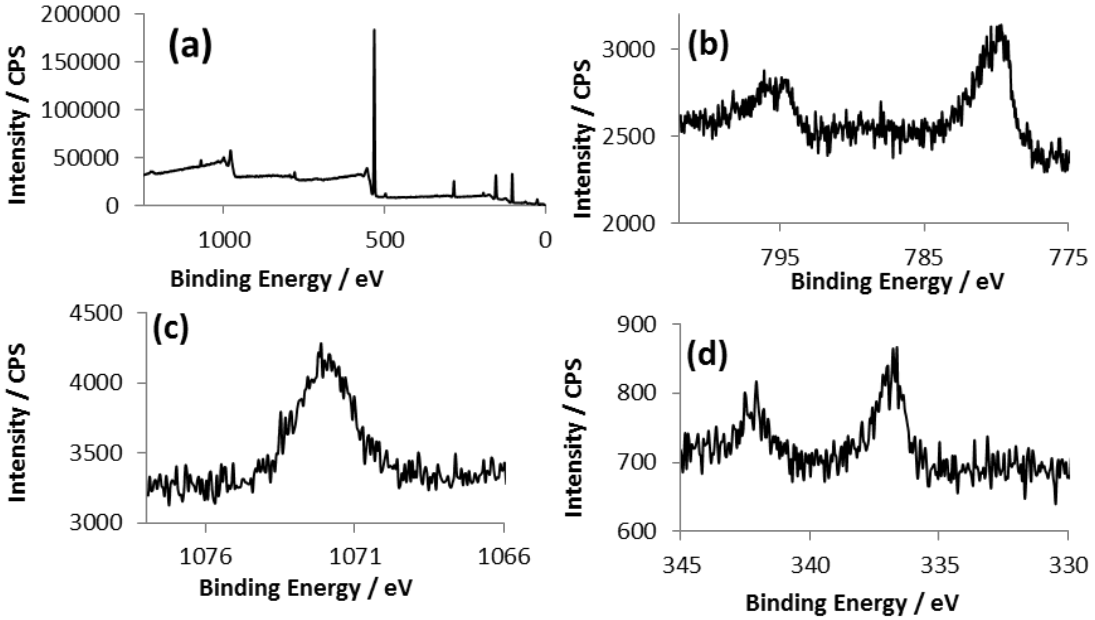

Figure 18. XPS spectra recorded for 20wt%Co/1wt%Pd/1wt%Na/SiO_2-500Å. (a) Survey spectrum. (b) Co 2p region showing the presence of Co as Co_3O_4. (c) Na 1s region (d) Pd 3d region showing the presence of Pd as PdO.

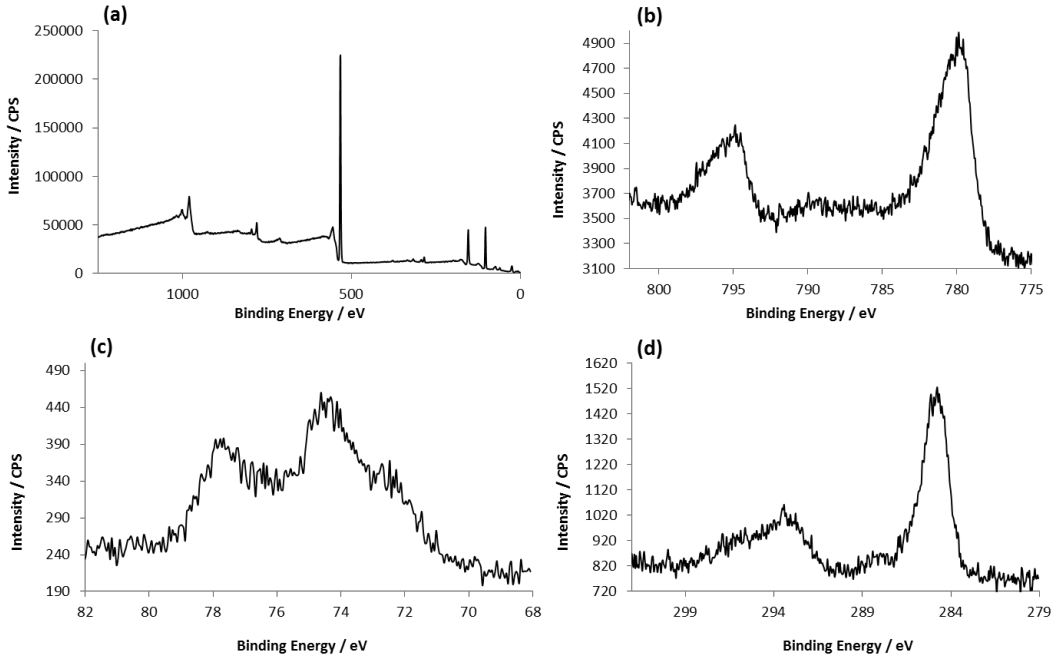

Figure 19. XPS spectra recorded for 20wt%Co/1wt%Pt/1wt%K/SiO_2-500Å. (a) Survey spectrum. (b) Co 2p region showing the presence of Co as Co_3O_4. (c) Pt 4d region indicating the presence of Pt as PtO_2 (d) K 2p region indicating the presence of K_2O. Note that the peak present at 284.7 eV is the C 1s peak and the smaller the peak at 293.07 eV is attributed to K 2p

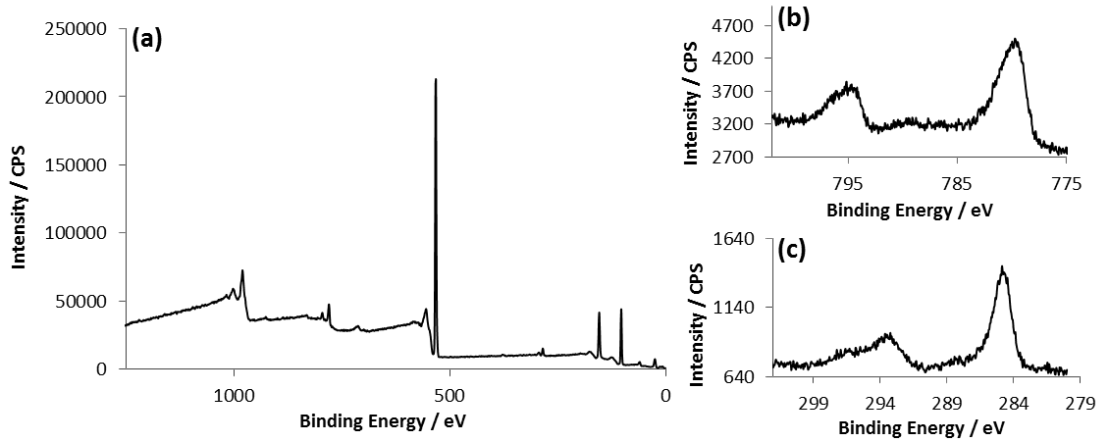

Figure 20. XPS spectra recorded for 20wt%Co/1wt%Ru/1wt%K/SiO_2-500Å. (a) Survey spectrum. (b) Co 2p region showing the presence of Co as Co_3O_4. (c) K 2p region indicating the presence of K_2O. Note that the peak present at 284.7 eV is the C 1s peak and the smaller the peak at 294.01 eV is attributed to K 2p. No peaks attributable to any ruthenium species could be detected.

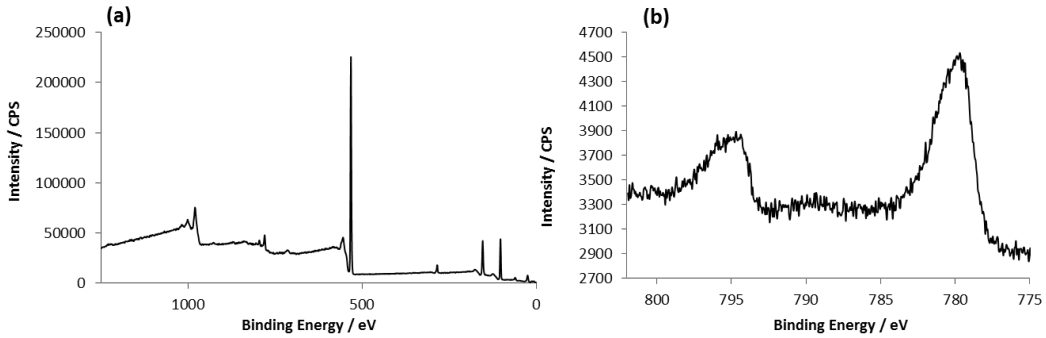

Figure 21. XPS spectra recorded for 20wt%Co/1wt%Li/SiO_2-500Å. (a) Survey spectrum. (b) Co 2p region showing the presence of Co as Co_3O_4. No peaks attributable to any lithium species could be detected.

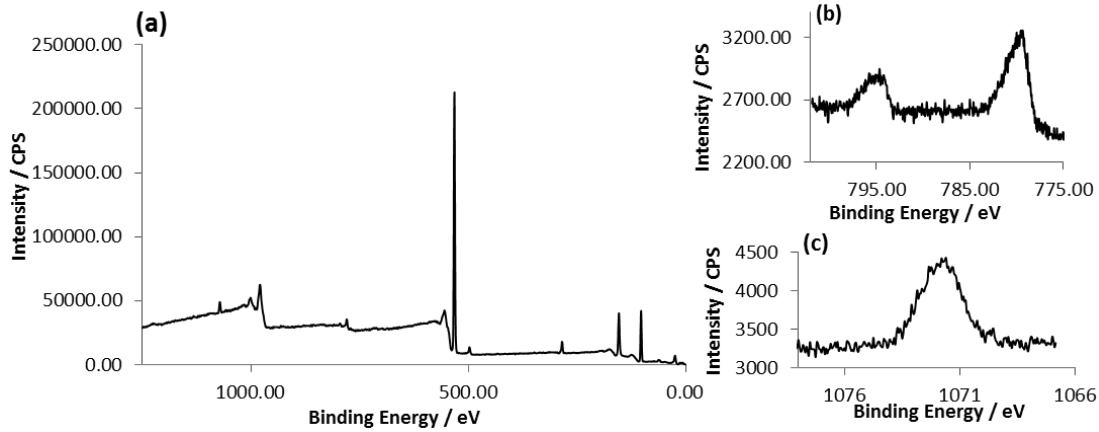

Figure 22. XPS spectra recorded for 20wt%Co/1wt%Na/SiO_2-500Å. (a) Survey spectrum. (b) Co 2p region showing the presence of Co as Co_3O_4. (c) Na 1s region.

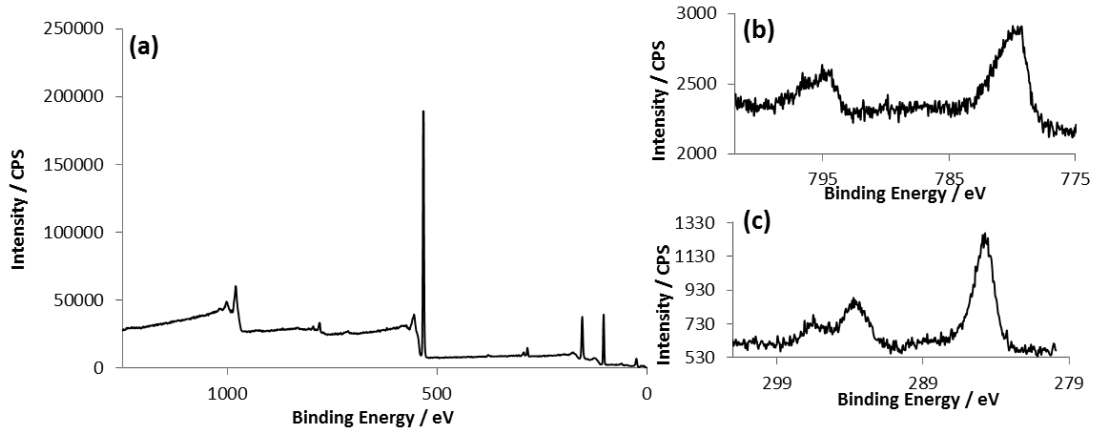

Figure 23. XPS spectra recorded for 20wt%Co/1wt%K/SiO_2-500Å. (a) Survey spectrum. (b) Co 2p region showing the presence of Co as Co_3O_4. (c) K 2p region indicating the presence of K_2O. Note that the peak present at 284.7 eV is the C 1s peak and the smaller the peaks at 292.91 eV are attributed to K 2p.

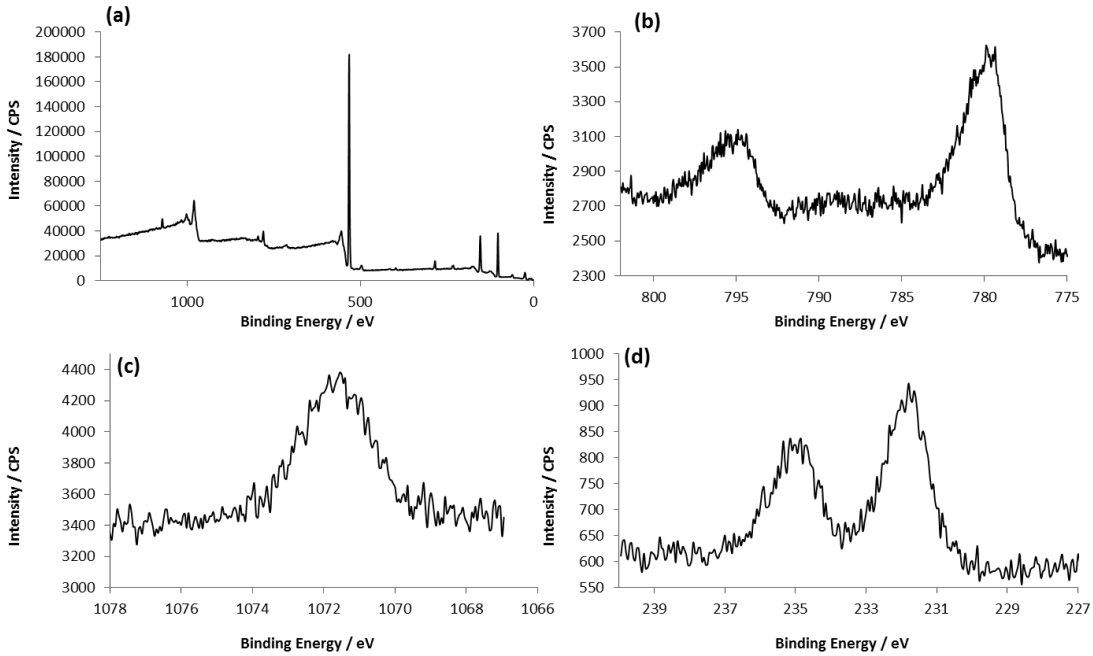

Figure 24. XPS spectra recorded for 20wt%Co/1wt%Na/1wt%Mo/SiO_2-500Å. (a) Survey spectrum. (b) Co 2p region showing the presence of Co as Co_3O_4. (c) Na 1s region (d) Mo 3d region indicating the presence of Mo in the MoO_3 form.

For all catalyst systems investigated by XPS no significant change in the binding energy of the cobalt component of the catalyst was observed. All suggest the presence of cobalt in its Co_3O_4 oxide form which is further confirmed by the pXRD measurements conducted. No change in cobalt oxidation state or binding energy is evident with the changing of catalyst support properties or the addition of any of the promoters studied within this paper.

Reaction Mechanisms

The hydrogenation of carbon dioxide is thought to proceed through one of three main mechanisms; (1) the direct hydrogenation of carbon dioxide for hydrocarbon formation,[2] (2) the conversion of carbon dioxide to methanol followed by the conversion of methanol to hydrocarbons *via* the methanol to gasoline (MTG) process[3] or (3) the reduction of carbon dioxide to carbon monoxide *via* the reverse water-gas shift (RWGS) reaction followed by the conversion of the formed carbon monoxide to hydrocarbons through the Fischer-Tropsch process.[4]

The lack of any methanol in the product stream suggests that CO_2 hydrogenation is not proceeding through this methanol mediated mechanism under the reaction conditions studied within this paper. The detection of carbon monoxide within the reaction stream does however suggest that the CO mediated RWGS – FT process is a possibility.

The Anderson Schulz Flory (ASF) distribution (Equation 1) describes the formation of hydrocarbons *via* the Fischer-Tropsch process.[5] If hydrocarbons are formed *via* the Fischer-Tropsch process a plot of carbon number (n) versus $log(w_n/n)$ should give a straight line with a gradient equal to $log(\alpha)$, where α is the chain growth probability as defined in Equation 2.

$$\log\frac{w_n}{n} = nlog(\alpha) + const$$

Equation 1 – The Anderson Schulz Flory distribution

$$\alpha = \frac{R_p}{R_P + R_t}$$

Equation 2 – Equation showing the relationship between α and rates of chain termination (R_t) and propagation (R_p)

Figure 25 shows ASF plots for selected catalysts systems, specifically those with a high selectivity towards heavier hydrocarbons. The straight line trend observed for these two catalyst systems suggests that CO_2 hydrogenation is indeed occurring *via* the RWGS reaction (CO is detected in the product stream) followed by the formation of hydrocarbons *via* the Fischer-Tropsch process as evidenced by the ASF plots.[6] A slight anomaly is observed for C_2 hydrocarbons, a common observation for Fischer-Tropsch catalysts.[7]

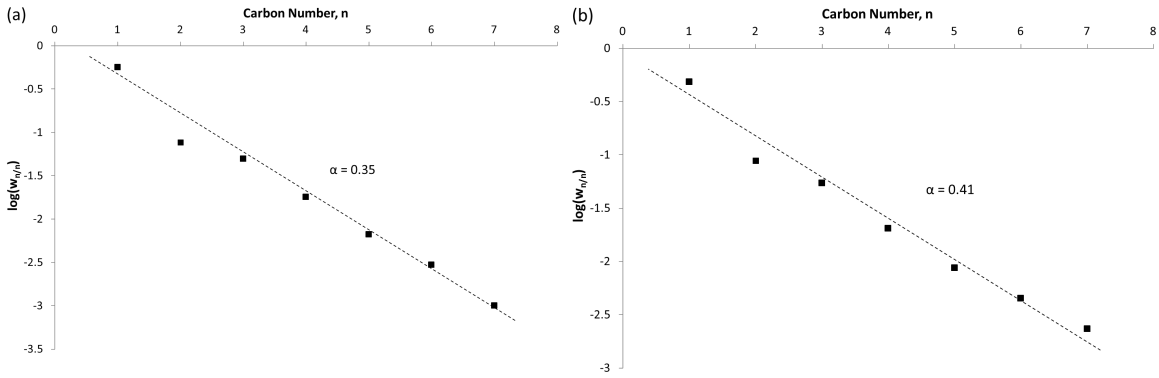

Figure 25. ASF plots for (a) 20wt%Co/1wt%Na/SiO_2-500 and (b) 20wt%Co/1wt%Na/1wt%Mo/SiO_2-500.

The RWGS shift reaction is thought to proceed through a redox mechanism as detailed in Scheme 1 where *a* represents a surface site.[8] The redox mechanism begins with the dissociative adsorption of carbon dioxide molecule to give a surface bound CO and O. Hydrogen present in the reaction mixture is also dissociatively adsorbed to give surface hydrogen species. The carbon monoxide then desorbs from the surface to give gaseous carbon monoxide and the oxygen reacts with the hydrogen species present to give water.[8]

$$CO_{2(g)} \rightleftharpoons CO_a + O_a$$
$$CO_a \rightleftharpoons CO_{(g)}$$
$$H_{2(g)} \rightleftharpoons 2H_a$$
$$H_a + O_a \rightleftharpoons OH_a$$
$$H_a + OH_a \rightarrow H_2O_a$$
$$H_2O_a \rightleftharpoons H_2O_{(g)}$$

Scheme 1. The redox mechanism for the WGS reaction.

While extensive experimental evidence supports this mechanism[8-9] there still remains great debate over the mechanism with the formate decomposition mechanism,[10] which is also well supported by experimental evidence,[11] still popular with many.

As with the RWGS reaction great debate still exists over the mechanism of Fischer-Tropsch process with 5 popular suggestions; the carbide mechanism,[12] the alkenyl/vinyl mechanism,[13] Dry's mechanism,[14] the enol mechanism[15] and the carbonyl insertion mechanism.[16] The lack of oxygenated products detected utilising the catalysts reported within this paper suggests that HC formation is unlikely to occur through the enol or carbonyl mechanism as oxygenated species form an integral part of both mechanisms, it is however possible that any oxygenated species are too short lived under these reaction conditions to be detected.[14]

The mechanism suggested by Dry[14] relies on the combination of two methylene species formed from the combination of surface carbide and hydride species giving a metallocylcopropane with a two point attachment to the surface (see Scheme 2) whereas all other mechanisms suggest a single point of attachment for the growing chain. Chain growth occurs *via* the insertion of a CH_2 monomer into one of the bonds between the growing chain and surface resulting in the formation of a metallocyclobutane which then rearranges to form a metallocyclopropane as shown in Scheme 2.

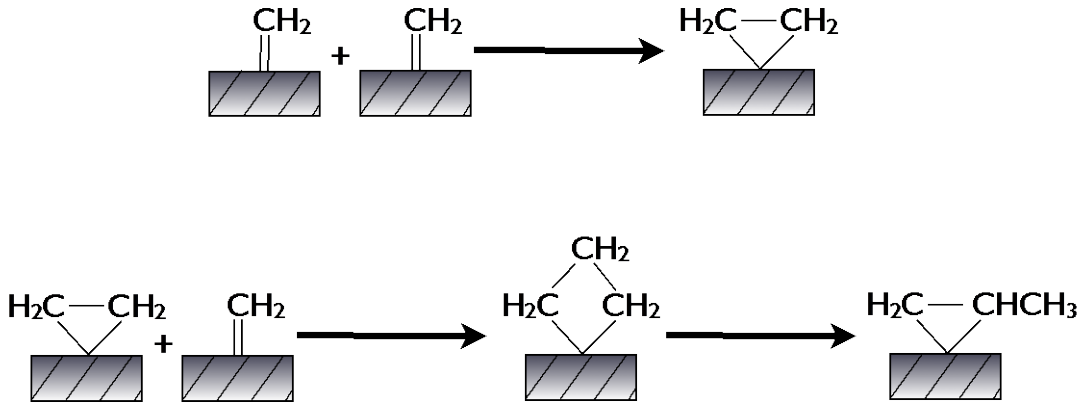

Scheme 2. The formation of metallocyclopropane followed by CH_2 insertion.[17]

With the insertion of a CH_2 group to the metallocyclopropane the two bonds attaching the growing chain to the surface metal site are no longer equal due to the increased steric bulk on one side (site b, see Scheme 3). This means that the next CH_2 monomer is more likely to insert at site a (see Scheme 3). Insertion at site b is however still possible as shown in Scheme 3, this results in the formation of a monomethyl branched hydrocarbon chain. This accounts for the predominantly monomethyl branching observed for the products of the Fischer-Tropsch process. The likelihood of insertion at site b decreases as the chain length increases which also agrees with the trend commonly observed in Fischer-Tropsch produced hydrocarbons where the degree of branching is lower with increasing chain length.

This reaction mechanism also provides an explanation for the lower than expected C_2 value for ASF as shown earlier (Figure 25) since C_2 species, such as that shown in Scheme 2, have two equally active bonds where CH_2 insertion can occur. For C_3 and higher hydrocarbons the steric bulk on one side of the growing chain reduces the probability of chain growth at that site, lowering the rate of chain growth relative to the C_2 species resulting in a slightly lower amount of C_2 products than predicted by the ASF distribution. None of the other mechanisms listed above are able to explain this phenomenon.

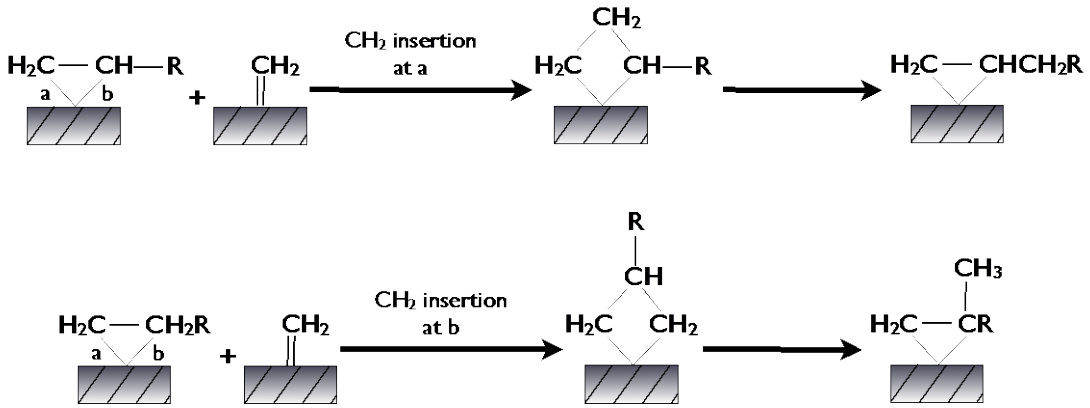

Scheme 3. CH_2 insertion at the two non-equivalent positions of the metallocyclopropane structure

Termination can occur by desorption of the growing chain giving a terminal olefin or by the hydrogenation of the metallocyclopropane species to give paraffins. Significantly more detailed studies outside the scope of this current study are however required to determine if hydrocarbon formation is occurring *via* this mechanism or another of the Fischer-Tropsch mechanisms mentioned previously.

For some of the catalyst systems containing cobalt, potassium and palladium supported on SiO_2-60 that produce high quantities of methane product distributions no longer follow the ASF distribution. Instead the double alpha phenomenon commonly seen with cobalt based catalysts when used for CO_2 hydrogenation[18] is observed as shown in Figure 26.

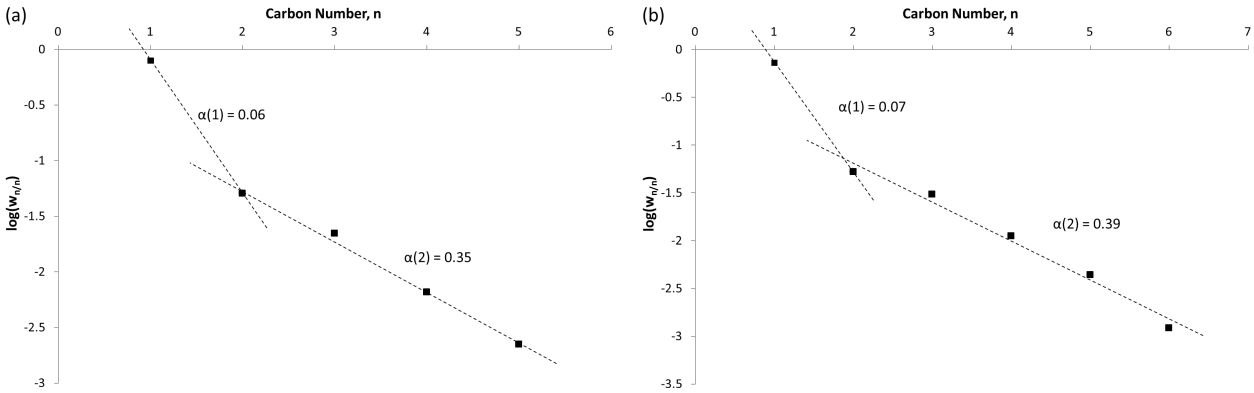

Figure 26. ASF plots for (a) 20wt%Co/1wt%Pd/1.5wt%K/SiO_2-60 and (b) 20wt%Co/1wt%Pd/3wt%K/SiO_2-60.

Methane content is higher than predicted by the ASF distribution and as such does not lie on the same trend line as the C_2+ hydrocarbon. The fact the C_2+ hydrocarbons produced do give a linear relationship and suggests that they are formed through the Fischer-Tropsch process. While some methane is likely formed *via* the Fischer-Tropsch process its higher than predicted content suggests that methane is being formed through another parallel process such as the direct hydrogenation of CO_2 to form CH_4 with no CO intermediate[19] through the equation:

$$CO_2 + 4H_2 \rightarrow CH_4 + 2H_2O$$

Again more detailed studies are needed to confirm this is the case.

References

[1] J.P. de Breejen, P.B. Radstake, G.L Bezemer, J.H. Bitter, V . Forseth, A. Holmen, K.P. de Jong, *J. Am. Chem. Soc*., **2009**, *131*, 7197-7203
[2] T. Riedel, G. Schaub, K.-W. Jun, K.-W. Lee, *Ind. Eng. Chem. Res.* **2001**, *40*, 1355-1363.
[3] X. Ni, Y. Tan, Y. Han, N. Tsubaki, *Catal. Commun.* **2007**, *8*, 1711-1714.
[4] T. Riedel, M. Claeys, H. Schulz, G. Schaub, S. S. Nam, K. W. Jun, M. J. Choi, G. Kishan, K. W. Lee, *Appl. Catal. A: Gen.* **1999**, *186*, 201-213.
[5] A. Tavakoli, M. Sohrabi, A. Kargari, *Chem. Eng. J.* **2008**, *136*, 358-363.
[6] M. Fujiwara, H. Ando, M. Matsumoto, Y. Matsumura, M. Tanaka, Y. Souma, *Chem. Letts.* **1995**, *24*, 839-840.
[7] a) J. R. Anderson, M. Boudart, *Catalysis: science and technology*, Springer-Verlag, **1981**, Chapter 4; b) R. B. Anderson, H. Kölbel, M. Rálek, The Fischer-Tropsch synthesis, Academic Press, **1984**.
[8] K.-H. Ernst, C. T. Campbell, G. Moretti, *J. Catal.* **1992**, *134*, 66-74.
[9] a) S.-I. Fujita, M. Usui, N. Takezawa, *J. Catal.* **1992**, *134*, 220-225; b) R. A. Hadden, H. D. Vandervell, K. C. Waugh, G. Webb*, Catal. Lett.* **1988**, *1*, 27-33.
[10] T. Salmi, R. Hakkarainen, *Appl. Catal.* **1989**, *49*, 285-306.
[11] a) C.-S. Chen, W.-H. Cheng, *Catal. Lett.* **2002**, *83*, 121-126; b) A. N. Pour, M. R. Housaindokht, S. F. Tayyari, J. Zarkesh, *J. Natural Gas Chem.* **2010**, *19*, 362-368.
[12] G. P. Van Der Laan, A. A. C. M. Beenackers, *Catal. Revs.* **1999**, *41*, 255-318.
[13] P. M. Maitlis, H. C. Long, R. Quyoum, M. L. Turner, Z.-Q. Wang, *Chem. Commun.* **1996**, 1-8.
[14] M. E. Dry, *Appl. Catal. A: Gen.* **1996**, *138*, 319-344.
[15] R. B. Anderson, R. A. Friedel, H. H. Storch, *J. Chem. Physics* **1951**, *19*, 313-319.
[16] E. de Smit, B. M. Weckhuysen, *Chem. Soc. Revs.* **2008**, *37*, 2758-2781.
[17] B. H. Davis, Fuel Processing Technology **2001**, *71*, 157-166.
[18] R. W. Dorner, D. R. Hardy, F. W. Williams, H. D. Willauer, *Energy & Environ. Sci.* **2010**, *3*, 884-890.
[19] T. Riedel, G. Schaub, K.-W. Jun, K.-W. Lee, *Ind. Eng. Chem. Res.* **2001**, *40*, 1355-1363.